Core/shell Cu/FePtCu nanoparticles with face-centered tetragonal texture: An active and stable low-Pt catalyst for enhanced oxygen reduction

Xu Chen, Hanbin Wang, Houzhao Wan, Tianci Wu, Dan Shu, Laifa Shen, Yi Wang, Pierre Ruterana, Peter Lund, Hao Wang

Nano Energy 54 (2018) 280–287

Contents lists available at ScienceDirect

Nano Energy

journal homepage: www.elsevier.com/locate/nanoen

Full paper

Core/shell Cu/FePtCu nanoparticles with face-centered tetragonal texture: An active and stable low-Pt catalyst for enhanced oxygen reduction

Xu Chen[a,b], Hanbin Wang[a], Houzhao Wan[a], Tianci Wu[a], Dan Shu[a], Laifa Shen[c], Yi Wang[c,*], Pierre Ruterana[b], Peter D. Lund[d,*], Hao Wang[a,*]

[a] Faculty of Physics and Electronic Science, Hubei Key Laboratory of Ferroelectric and Dielectric Materials and Devices, Hubei University, 430062 Wuhan, China
[b] CIMAP UMR 6252, ENSICAEN, 6 Boulevard Maréchal Juin, F-14050 Caen, France
[c] Max Planck Institute for Solid State Research, Heisenbergstr. 1, D-70569 Stuttgart, Germany
[d] Department of Applied Physics, Aalto University, PO.Box 15100, FI-00076 Aalto, Espoo, Finland

ARTICLE INFO

Keywords:
Oxygen reduction reaction
Stability
Activity
Core–shell structure
Face-centered tetragonal
FePtCu

ABSTRACT

Low-Pt based nanocrystals demonstrate potential as highly active catalysts for the oxygen reduction reaction (ORR), but they suffer from undesirable structural degradation. Therefore, it is highly challenging to optimize their surface and interfacial structures to tune their catalytic properties for both activity and stability. Here core–shell Cu/FePtCu nanoparticles with a face-centered-tetragonal phase are prepared by a facile one–pot polyol method at 320 °C. The optimized core–shell $Fe_{45}Pt_{35}Cu_{20}$ catalyst with Pt-enriched surface exhibits 0.5 A/mg_{Pt} mass activity, which is a factor of 4 better than that of commercial Pt/C (0.13 A/mg_{Pt}). In addition, the current density of the catalyst drops only 3.0% after 1000 cycles, which is much better than Pt/C (34.2% decay). Using aberration-corrected scanning transmission electron microscopy and atomically resolved elemental mapping, the morphology and structure evolving between the FePtCu alloy and core–shell Cu/FePtCu could clearly be explained. This work demonstrates that an ordered and core–shell FePtCu catalyst is highly promising for ORR and other electrochemical processes.

1. Introduction

Modern electrochemical energy conversion technologies such as proton-exchange-membrane (PEM) fuel cells have attracted much attention for transportation and stationary power applications, because of their high-energy conversion efficiency, low emissions, low-temperature operation and plentiful fuel sources [1–5]. It is well known that the PEM technology is constrained by the kinetically limited oxygen reduction reaction (ORR) at the cathode as well as the use of costly platinum (Pt) as the electro-catalyst [6–9]. Fine tuning of Pt-based nanocrystals [10–14], or replacing Pt with nonprecious materials has extensively been investigated in order to improve the catalysis performance for the ORR [15–18]. Because of stability issues of the cathode in an acidic and electrochemical environment, nonprecious metal catalysts are not yet available for the fuel cell industry [19,20]. Therefore, using highly active and stable Pt-based catalysts for ORR is a state-of-the-art solution in PEM fuel cells. As further direction, three categories of advanced Pt-based ORR catalysts can be developed, i.e., shaped Pt nanostructures, Pt-based alloys, and Pt-based core–shell structures [20–24]. It is believed that the origin of activity enhancement is mainly the modification of the surface structure and surface electronic state of Pt atoms.

Alloy catalysts with low-Pt content usually show a superior performance compared to pure Pt [25–27]. Numerous research efforts have indicated that the ORR performance of Pt catalysts can be improved by alloying Pt with 3d transition metals such as Fe, Cu, Co and Ni [28–33]. Stamenkovic et al. demonstrated that a monocrystalline extended surface of $NiPt_3$ (111) film possesses a specific activity of ORR that is 90 times higher than that of the benchmark Pt nanoparticles (NPs) [34]. Later major efforts have been made on shaped alloy nanostructures with specific facets [35–37]. However, Pt alloys are thermodynamically unstable under acidic and electrochemical conditions [19]. Core–shell structures is an alternative to improve the utilization of Pt atoms by depositing or forming a thin Pt shell around a less expensive core [38–41]. An appropriate Pt-skin thickness and modulated subsurface structure induces geometric and electronic effects that enhance the ORR activity. In general, the core–shell Pt nanostructure is an optimal choice because it can achieve a balance between low cost, high activity, and high stability.

Among these catalysts, the FePt alloy is proved to be efficient with

* Corresponding authors.
E-mail addresses: y.wang@fkf.mpg.de (Y. Wang), peter.lund@aalto.fi (P.D. Lund), wangh@hubu.edu.cn (H. Wang).

https://doi.org/10.1016/j.nanoen.2018.10.034
Received 21 September 2018; Received in revised form 15 October 2018; Accepted 15 October 2018
Available online 18 October 2018

improved activity, stability and low Pt content [33,42]. The catalytic performance of the FePt alloy NPs is strongly dependent on their crystalline structure [38,43,44]. For instance, when as-synthesized face-centered cubic (*fcc*) FePt NPs are exposed into acid electrolyte and electrochemical environment, Fe atoms can fast be etched out of FePt alloy NPs, which significantly reduces the activity and stability of surface Pt atoms due to losing of the Fe alloy effect. While, the stability and activity of the FePt catalysts can be dramatically improved once the Fe and Pt are in a chemically ordered face–centered tetragonal (*fct*) structure, namely, $L1_0$ or intermetallic structure. Sun et al. investigated the structure–dependent FePt NPs catalysis and demonstrated that *fct*–FePt NPs have much better ORR performance than the *fcc*–FePt and Pt/C [33]. The *fcc*–FePt has similar ORR onset potentials than commercial Pt/C, but the *fct*–FePt reduces this potential by nearly 100 mV. Besides, the half–wave potential decreased by 27% for *fcc*–FePt and 20% for Pt/C after 1000 cycles, but the decrease was much lower for *fct*–FePt, or 14%. This demonstrates that a phase transform into the *fct* structure is an effective way to enhance the catalytic efficiency of FePt NPs for ORR. Furthermore, *fct*–FePtCu/Pt NPs are found more efficient than *fct*–FePt/Pt, showing nearly 10 times higher specific activity than Pt/C [45].

Here we report a high active and stable ORR catalyst of *fct*–FePtCu NPs prepared by a facile one–pot method, which is a much simpler process than previously reported [45]. The intermetallic FePtCu NPs can be constructed with a wide controllable composition, i. e., 10∼40% for Cu and 30∼50% for Fe/Pt. Furthermore, as a proof of a concept that high performance *fct*–FePt ORR catalyst is not only ordered but also a core–shell structure. To our knowledge, this is the first time that an ORR catalyst with a core–shell structure and ternary $L1_0$ alloy shell is reported. The $Fe_{45}Pt_{35}Cu_{20}$ with a core–shell Cu/FePtCu structure shows an ORR catalysis performance, which is 4 times better in mass activity than commercial Pt/C. In addition, the current density decade only 3.0% after 1000 cycles, which is much better than with Pt/C (34.2% decay) and with previously reported face-center-tetragonal FePt (14.0% decay). We demonstrate that the facile one–pot synthesis of core–shell structure $L1_0$–FePtCu catalyst is highly promising for ORR and other electrochemical processes.

2. Experimental section

2.1. FePtCu NPs preparation

The preparation of ternary FePtCu is similar with our previous reported paper and can be summarized as follows [46,47]. (i) Firstly, at a temperature of 80 °C, hexadecylamine was melted into 20 ml liquid in a 100 ml flask container with four necks. Then, the solution was kept bubbling with nitrogen. (ii) After bubbling for 30 min and keep the temperature at 80 °C, reaction precursors were resolved into the hexadecylamine solvent under mechanical stirring, including 0.45–0.30 mmol $Pt(acac)_3$, 0.45–0.30 mmol $FeCl_2$, 0.10–0.40 mmol $Cu(acac)_2$, 1.5 mmol of 1,2–hexadecanediol, 1 ml oleic acid and 1 ml oleylamine. (iii) After that, the solution temperature was gradually heated to 320 °C at a heating rate of 10 °C/min. At around 240 °C, the colour of the solutions turns from blue into black. (iv) After refluxing at 320 °C for three hours, the heating source was removed so that the prepared black solutions cooled down naturally. Then, the N_2 bubbling and mechanical stirring could be removed. (v) Finally, the as-prepared black powder was washed by dispersing into hexane, precipitating with ethanol and centrifuging for three times at 5000 r/min. The final clean FePtCu products were dispersed in hexane for preservation. Two sets of FePtCu particles are prepared. One is with the same ratio of Fe and Pt, while with different Cu concentration, i. e., $(FePt)_{100-x}Cu_x$ (x = 10, 20, 30 and 40). The other is with fixed 20% Cu doping but different Fe and Pt ratio, i.e., $Fe_xPt_{80-x}Cu_{20}$ (x = 30, 35, 40, 45 and 50). X–ray Fluorescence (XRF) tests show that the prepared products have very similar composition as their precursors, so we can name these as–made NPs with precursor compositions for convenience.

2.2. Nanoparticle characterization

X–ray diffraction (XRD, Bruker D8) was used to characterize the FePtCu crystal structure. A physical property measurement system (PPMS) was adopted to measure the magnetic properties of the FePtCu NPs. A scanning transmission electron microscopy (STEM, JEOL ARM 200F) was used to characterize the morphology, microstructure and elemental distribution of FePtCu NPs. The microscope is equipped with both probe and image Cs correctors, and a large solid angle SDD–type EDX detector. High angle annular dark field (HAADF) imaging with high spatial resolution, high elemental resolution electron-energy-loss-spectroscopy (EELS) and energy-dispersive X-ray spectroscopy (EDXs) spectra were conducted to analysis the atomic structure of FePtCu. QSTEM image simulation software was also used to simulate the STEM image, using a model of 10 nm of $L1_0$–FePtCu. XRF was conducted to measure the composition of the FePtCu NPs. A scanning electron microscope (SEM, JSM7100F) was also used to characterize the size and morphology of the NPs.

2.3. Electrochemical measurements

For synthesizing catalyst colloids, as–synthesized FePtCu NPs and carbon black (Vulcan XC–72 R, Cabot) were mixed in hexane with a normalized mass ratio of 33.3% of platinum. After being sonicated for more than 1 h to form uniform colloidal, FePtCu/C catalyst was obtained. Ethanol was added into FePtCu/C hexane solutions followed by centrifuging for three more times to clean the particle surface. After that the FePtCu/C catalysts were dispersed into 1 ml isopropanol with 10 μL Nafion and sonicated for another 1 h to form a uniform colloid. Commercial Pt/C (20% of platinum loading, Sigma) catalyst was prepared according to literature method [33,42], i. e., by suspending it in deionized water, isopropanol and Nafion mixture solution with volume ratio of 4:1:0.05. Then, FePtCu/C catalysts along with commercial Pt/C were deposited on glassy carbon rotation disk electrode (Pine Instrument). Their catalytic ORR performance electrochemical were evaluated then in 0.5 M H_2SO_4 electrolyte with argon gas or oxygen gas saturated condition. For the measurement of the electrochemical properties of these as–prepared electrodes, Linear Sweep Voltammetry and Cyclic Voltammetry (CV) techniques were used by a computer controlled electrochemical workstation (CHI660D), which comprised one of the as–fabricated FePtCu or Pt/C electrodes as the working electrode. We use an Ag/AgCl reference electrode and a Pt-wire counter electrode.

3. Results and discussion

Fig. 1a shows a schematic illustration the effect of Cu doping on the size, solid-solution alloy structure (denotes as alloy in this manuscript), and core–shell structure evolutions of FePtCu nanoparticles. The insets are EELS mapping images of a single alloy/core–shell particle for intuitive illustration, and the corresponding large-area-mapping images can be seen in Fig. S1 in Supporting information. With 10% Cu, the particle diameter ranges from 11.1 nm to 24.2 nm, as shown by the particles size analysis in Fig. 1b. FePtCu shows sphere morphology with mean diameter of 16.1 nm. Fe, Cu, and Pt atoms are well dispersed through these particles, demonstrating alloy structure by the EDXs line scan analysis. When the share of Cu increases to 20%, the particles grow bigger with particle diameter ranging from 17.8 to 43.1 nm (mean diameter 32.7 nm, Fig. 1c). Meanwhile, the EDXs line scan profile shows that Cu aggregates into the core of the FePtCu NPs resulting in a Cu–rich core and a FePt–rich shell structure. The core–shell structure was validated by a large area elemental mapping image. When the Cu composition was increased to 40%, FePtCu NPs are mostly sintered as Cu doping lowers the melting temperature of this alloy NPs, which

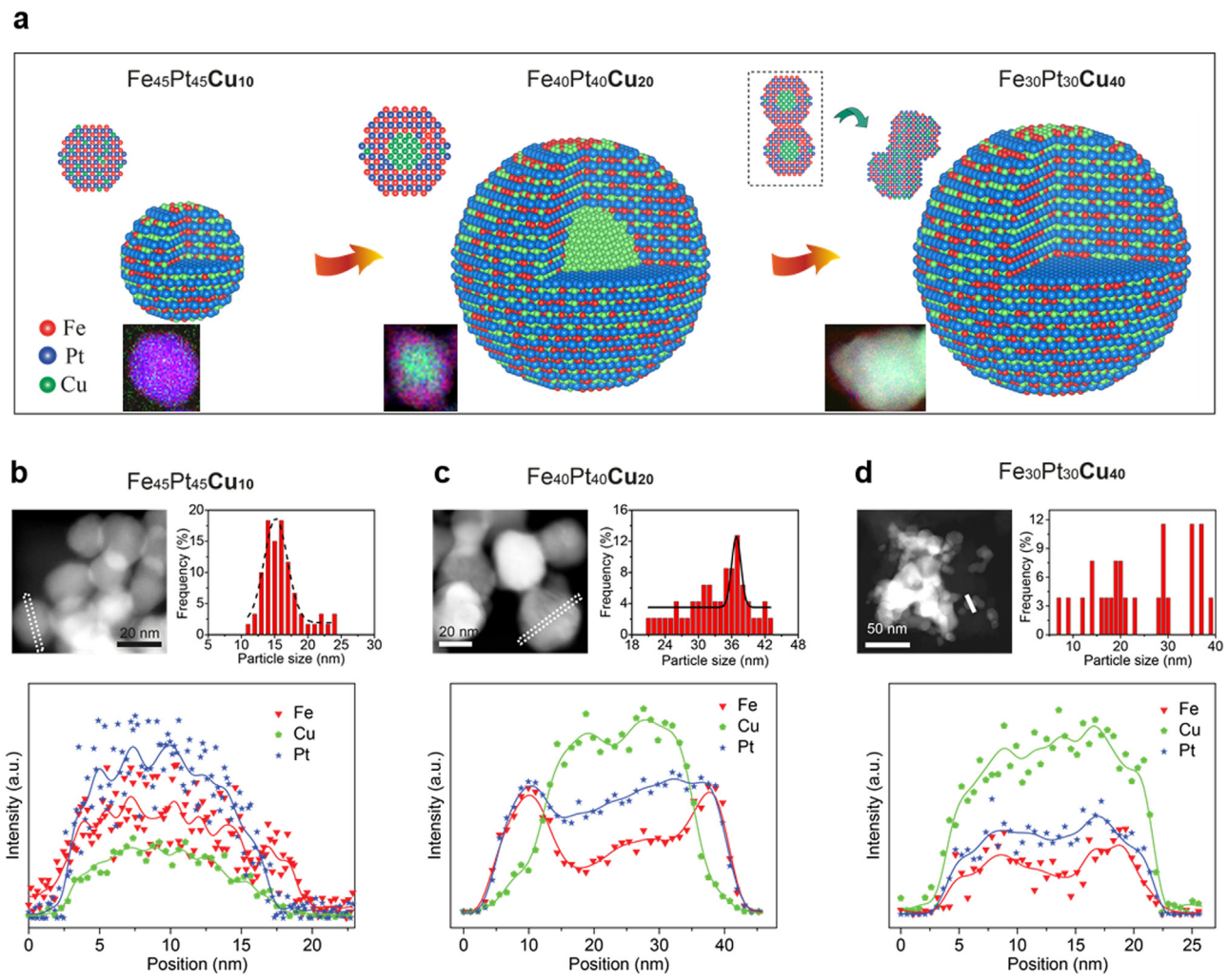

Fig. 1. a) Schematic illustration of FePtCu composition effect on their morphology and structure evolution from alloy to core–shell. HAADF-STEM image, diameter distribution, and EDX line-scan profiles of the particle marked in white colour to the STEM image for b) $Fe_{45}Pt_{45}Cu_{10}$, c) $Fe_{40}Pt_{40}Cu_{20}$ and d) $Fe_{30}Pt_{30}Cu_{40}$, respectively.

leads to an alloy structure caused by atom diffusion. The particle size distribution becomes widely dispersed (diameter of non-aggregated particles is shown in Fig. 1d). For the morphology evolution, low-magnification SEM and TEM images of these three FePtCu compositions are shown in Fig. S2(Supporting information). The high–resolution TEM images all show good crystallization and clear (001), (110), and (111) lattices which well match with $L1_0$–FePtCu demonstrating that the Cu alloy in FePt promotes the phase transformation from *fcc* to *fct* structure.

The alloy effect is supported by XRD analysis of $(FePt)_{100-x}Cu_x$ (x = 10, 20, 30 and 40) NPs with standard $L1_0$ FePt/FePtCu XRD spectra as reference shown in Fig. 2. The four samples show very similar peaks, which can be well assigned to (001), (110), (111), (200), (002), (201), (112), (220), and (202) peaks of *fct*–FePtCu (PDF No. 26–528) based on the XRD analysis. The occurrence of the characteristic $L1_0$ superlattice peaks at around 24.1° (001) and 32.9° (110) indicates that the Cu additive can efficiently promote the phase transformation at these concentrations. In order to investigate the Cu doping effect on the FePtCu ordering, we carried out refined XRD analysis shown in Fig. 2b. For $Fe_{45}Pt_{45}Cu_{10}$ with low Cu content, the (001), (110), and (111) peaks well match with *fct*–FePt (PDF No. 43-1359). With an increasing Cu concentration, the (001) and (111) peaks shift to higher 2θ degree, whereas the (110) peaks shift to lower 2θ degree, gradually approaching the *fct*–FePtCu (PDF No. 26-528) peaks. It is well known that an expansion of the FePt lattice *a*–axis is accompanied with a contraction of the FePt *c*–axis along with the additive content increasement, which promotes the $L1_0$ ordering process. Besides, another $L1_0$ superlattice (002) peak gradually arises when the Cu concentration is higher than 20%. Based on the above XRD analysis, we conclude that the *fct*–FePtCu alloy NPs are synthesized as a result and that the Cu alloy effect is the driving force for this ordering transformation. To evaluate the electrocatalytic activities for ORR, FePtCu NPs were supported on carbon black as catalyst and commercial Pt/C catalyst was prepared for reference. Before the ORR kinetics measurements, all catalysts were subject to potential cycling in N_2 saturated 0.5 M H_2SO_4 electrolyte until the curves became stable (all electrochemical potentials in this manuscript were converted to the reversible hydrogen electrode (RHE), Fig. S3 in Supporting information). Fig. 2c shows the CV curves for FePtCu and Pt/C catalysts in O_2–saturated electrolyte at 50 mV/s. Characteristic adsorption/desorption processes of under–potentially deposited H_{upd} at low potential of –0.05 to 0.30 V and hydroxyl layer on the catalyst surface at potential of 0.60–0.70 V were clearly seen. The catalytic activity of $Fe_{40}Pt_{40}Cu_{20}$ NPs is apparently higher than that of the other FePtCu compositions due to its higher OH_{ad} reduction current peak at 0.6 V. Fig. 2d shows the ORR polarization curves for the four catalysts and Pt/C by using rotation disk electrode linear voltammetry. $Fe_{40}Pt_{40}Cu_{20}$ NPs show the highest onset potential among the four catalysts demonstrating that the core–shell structure FePtCu enhances the catalytic performance of FePtCu.

As the structure and ORR performance of alloy catalysts are strongly

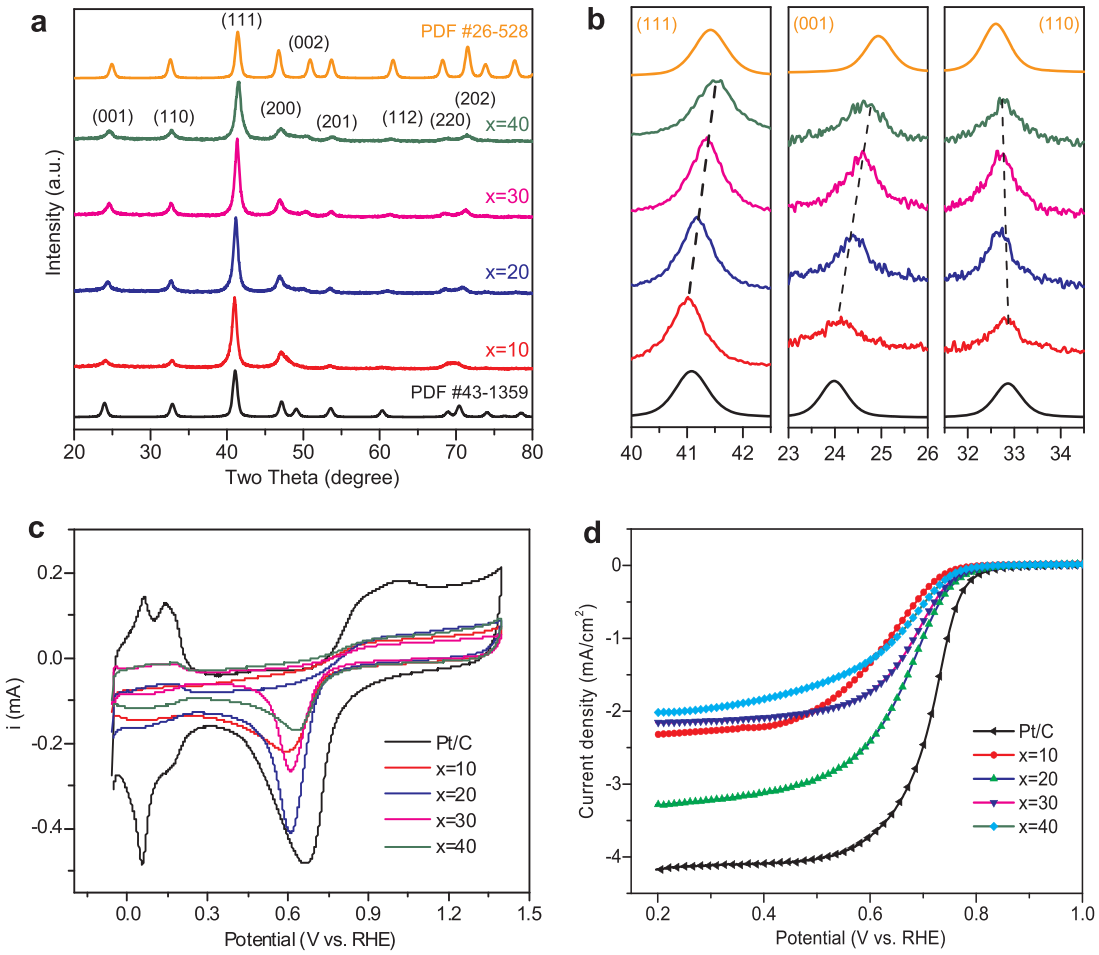

Fig. 2. a) XRD spectra of the as-synthesized $(FePt)_{100-x}Cu_x$ (x = 10, 20, 30 and 40) NPs. b) Enlarged sections of the (001), (110), and (111) peaks for the 2θ range of 23°~26°, 31°~35°, and 40°~43°. c) CV curves of $(FePt)_{100-x}Cu_x$ and commercial Pt/C at 50 mV/s in O_2 saturated 0.5 M H_2SO_4 electrolyte, and (d) ORR polarization curves.

affected by alloy composition, we adjusted the Fe and Pt ratio as $Fe_xPt_{80-x}Cu_{20}$ to optimize the catalytic performance. The XRD spectra (Fig. 3a) of FePtCu NPs synthesized in various Fe/Pt ratios and fixed to 20% Cu content resemble those of $(FePt)_{100-x}Cu_x$ NPs and with $L1_0$ phase. The $Fe_xPt_{80-x}Cu_{20}$ peaks are between $L1_0$–FePt and $L1_0$–FePtCu, which can be more clearly observed in the (110), (001), and (111) peaks shown in Fig. 3b. When the Fe content is decreased from 50% to 30%, the (001)/(110) peaks of as–synthesized $Fe_xPt_{80-x}Cu_{20}$ NPs are barely shifted, and the (111) peaks are slightly shifted toward lower diffraction angle, which means that the lattice parameter increases. This is reasonable due to a larger unit cell of Pt (9.1 cm^3/mol) than Fe (7.1 cm^3/mol). We also characterized the magnetic properties of $Fe_xPt_{80-x}Cu_{20}$ NPs to prove the phase transformation (Fig. S4 in Supporting information). For $Fe_{30}Pt_{50}Cu_{20}$ NPs, the hysteresis loop shows two–phase behavior, which means that a partially ordered FePtCu phase was formed in this composition with a coercivity of 0.9 kOe. When the Fe contents was increased to 35%, the coercivity of the NPs increased to 4.80 kOe indicating that the NPs contain a hard magnetic FePtCu phase. Further increase of the Fe contents yielded 2.1 kOe, 3.6 kOe, and 3.1 kOe coercivity for $Fe_{40}Pt_{40}Cu_{20}$, $Fe_{45}Pt_{35}Cu_{20}$, and $Fe_{50}Pt_{30}Cu_{20}$ NPs, respectively. Thus, the as–synthesized FePtCu NPs are ferromagnetic, due to the Cu–alloying effect and the phase transition of FePt [48–51]. Besides, the FePtCu NPs with various atom ratios have different ordering degree and surface structure due to the composition effect, which is also important for catalysis. Fig. 3c shows the ORR polarization curves of $Fe_xPt_{80-x}Cu_{20}$ NPs, in which the $E_{1/2}$ values of the alloys correspond to the following order: $Fe_{45}Pt_{35}Cu_{20}$ > Pt/C ≥ $Fe_{40}Pt_{40}Cu_{20}$ > $Fe_{30}Pt_{50}Cu_{20}$ ≥ $Fe_{50}Pt_{30}Cu_{20}$ > $Fe_{35}Pt_{45}Cu_{20}$, with values of 0.71, 0.70, 0.70, 0.66, 0.66, and 0.64 V (vs. RHE), respectively. Moreover, the onset potential of $Fe_{45}Pt_{35}Cu_{20}$ was reduced by nearly 40 mV compared to that of Pt/C. Fig. 3d shows the mass activities measured at half wave potential. The currents were normalized to the electrochemically active surface area (ECSA) of each catalyst, which was calculated by measurement of the columbic charge for hydrogen under-potential desorption in the CVs (Fig. S5a in Supporting information). The mass activity shows the same sequence as the $E_{1/2}$ values and $Fe_{35}Pt_{45}Cu_{20}$ NPs exhibited comparable mass activity with a value of 0.50 A/mg_{Pt}, which is 4 times higher than that of commercial Pt/C. Furthermore, the as–synthesized $Fe_{45}Pt_{35}Cu_{20}$ catalyst is superior to the commercial Pt/C and can save 74.3% of Pt at a potential of 0.7 V. We measured the ORR polarization curves of $Fe_{45}Pt_{35}Cu_{20}$ at different rotation speeds, i.e., 400, 900 and 1600 rpm, respectively, as shown in Fig. 3e. Then we can calculate the electron transfer number (n) according to the Koutecky–Levich equation [52,53]:

$$\frac{1}{j} = \frac{1}{j_k} + \frac{1}{j_l} = \frac{1}{j_k} + \frac{1}{B}\omega^{-1/2} \quad (1)$$

$$B = 0.62nFcD^{2/3}\nu^{-1/6} \quad (2)$$

where j is the current density (A/cm^2), F is Faraday constant (96485 C/mol), c is O_2 concentration (1.26×10^{-6} mol/cm^3), D is the diffusion coefficient (1.9×10^{-5} cm^2/s), and ν is the viscosity of the electrolyte (1.009×10^{-2} cm^2/s). Fig. 3f shows the j^{-1} versus $\omega^{1/2}$ plots at 0.6 V, 0.7 V, and 0.8 V for $Fe_{45}Pt_{35}Cu_{20}$ nanoparticles. The number of electrons calculated from the slope is 3.6, which demonstrates that it is

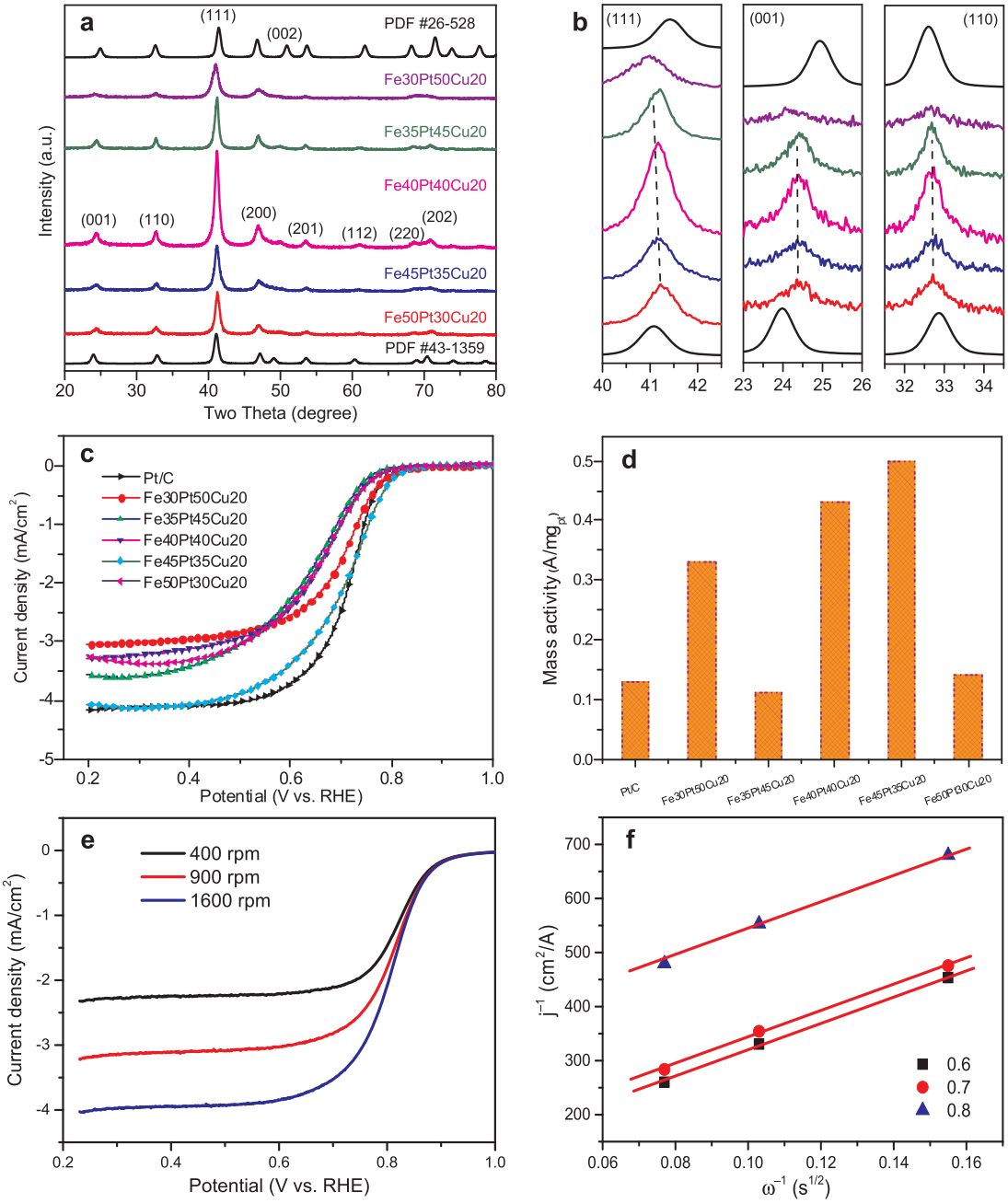

Fig. 3. a) XRD spectra of the as-synthesized $Fe_xPt_{80-x}Cu_{20}$ (x = 30, 35, 40, 45 and 50) NPs. b) Enlarged sections of the (001), (110), and (111) peaks for the 2θ range of 23°~26°, 31°~35°, and 40°~43°. c) ORR polarization curves of $Fe_xPt_{80-x}Cu_{20}$ and commercial Pt/C. d) Calculated ORR mass activites. e) Rotation-rate dependent current–potential curves for $Fe_{45}Pt_{35}Cu_{20}$. f) The calculated Koutecky-Levich curves at 0.6, 0.7, and 0.8 V for $Fe_{45}Pt_{35}Cu_{20}$.

mainly about a four-electron transfer process of FePtCu. The stability of the $Fe_{45}Pt_{35}Cu_{20}$/C catalyst for ORR was tested between 0.6 and 1.0 V in N_2–saturated 0.5 M H_2SO_4 with a scan rate of 100 mV/s. The CV and ORR polarization curves of the $Fe_{45}Pt_{35}Cu_{20}$ NPs before and after 1000 cycles (Fig. S6 in Supporting information) showed a slight 3.0% decay of the current density at the half–wave potential demonstrating sufficient stability. The current density of the Pt/C benchmark catalyst decays 34.2% and the previously reported face-center-tetragonal FePt decays 14.0% under the same electrochemical conditions [33].

It is well known that the surface Pt atoms play a key role in Pt–based catalysts for ORR, because electrochemical adsorption/desorption of oxygenated species react at the surface. Therefore, the change of catalyst composition will reflect in their ORR activities indicated by the studies on FePt, PtRu, and PdSe systems [54–56]. According to the equilibrium phase diagram of Fe–Pt–Cu, the ternary FePtCu alloy shows two ordered phases of $L1_2$ (cubic) and $L1_0$ (tetragonal), which are also related to the iron, platinum and copper composition [57]. To characterize the composition and structure effects on the catalytic performance, as-fabricated $Fe_{45}Pt_{35}Cu_{20}$ NPs were investigated by HAADF-STEM and EDXs mapping analysis as shown in Fig. 4b (see also Fig. S7 for more mapping results). The diameter of the NPs range from 17.8 to 37.9 nm and the mean diameter is 28.7 nm. The elemental mapping provides clear evidence of the core–shell structure. However, if the Fe/Pt ratio deviates too much from the optimal one, it results in significant change of the morphology and structure of FePtCu NPs shown in Fig. 4a,c. The $Fe_{30}Pt_{50}Cu_{20}$ has a uniform nanoparticle size ranging from 11.1 to 24.0 nm, with a mean diameter of 16.7 nm, which is smaller compared to the NPs with 45% iron (Fig. 4b). Decreasing the Fe

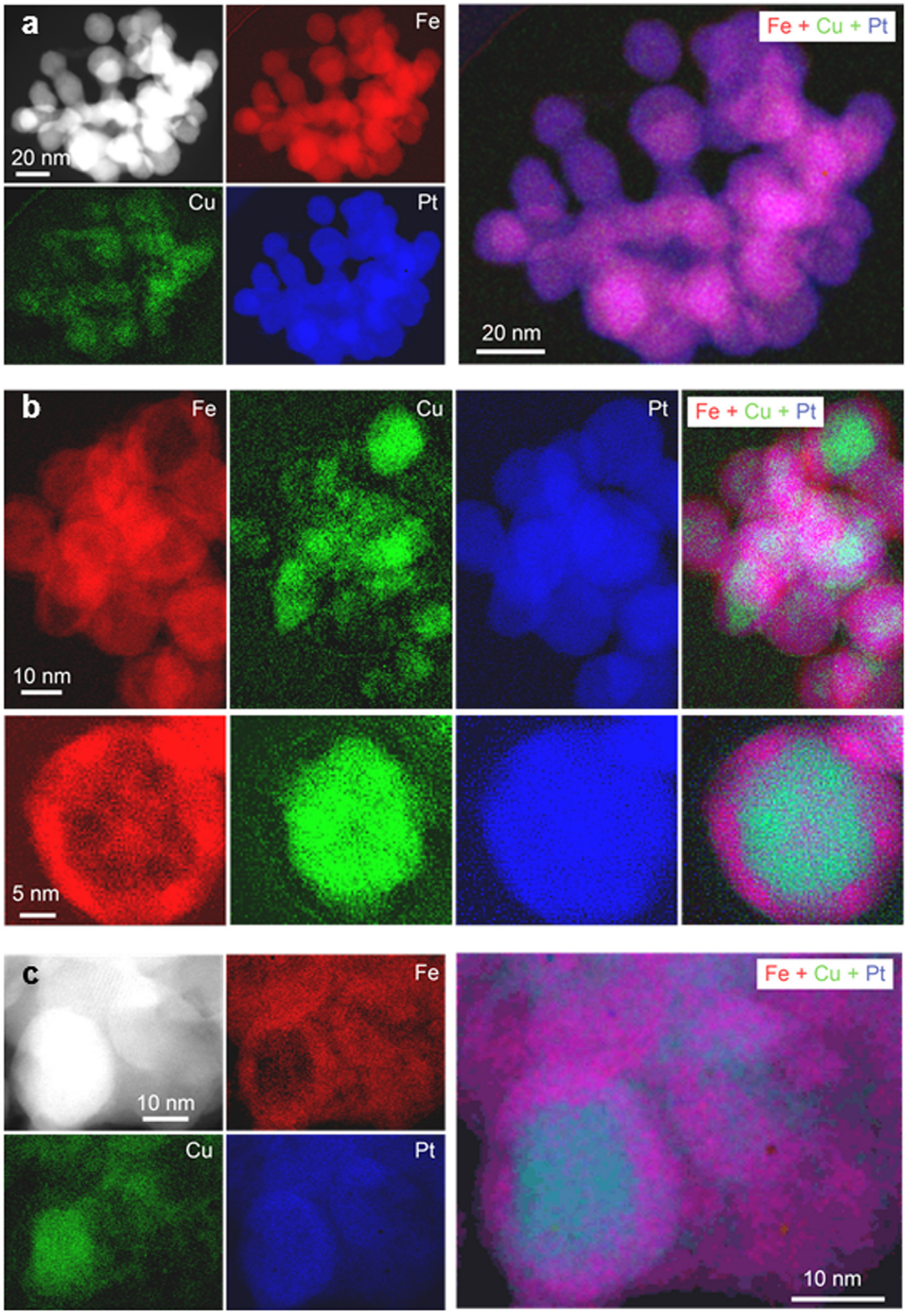

Fig. 4. a) HAADF-STEM image of $Fe_{30}Pt_{50}Cu_{20}$ and EELS elemental mapping of Fe (red), Cu (green), Pt (blue) and their overlap. b) Elemental distribution analysis of $Fe_{45}Pt_{35}Cu_{20}$. c) Elemental distribution analysis of $Fe_{50}Pt_{30}Cu_{20}$.

content to 30% results in an alloy structure demonstrating that the Fe content is also critical for the formation of alloy and core–shell structures. For $Fe_{50}Pt_{30}Cu_{20}$, a low magnification TEM image shows that the particles were sintered with diameters ranging from 13.0 to 38.2 nm. The EELS spectrum of $Fe_{50}Pt_{30}Cu_{20}$ in Fig. 4c shows that it is accompanied with a partial Cu@FePtCu core–shell structure with a Cu–rich core and a FePt–rich shell. Increasing the Fe content from 45% to 50% makes the particles partial core–shell caused by sintering induced atom diffusion. Characteristic $L1_0$ lattices of (001), (110) planes of planes of FePtCu can be found for $Fe_{35}Pt_{45}Cu_{20}$ and $Fe_{50}Pt_{30}Cu_{20}$

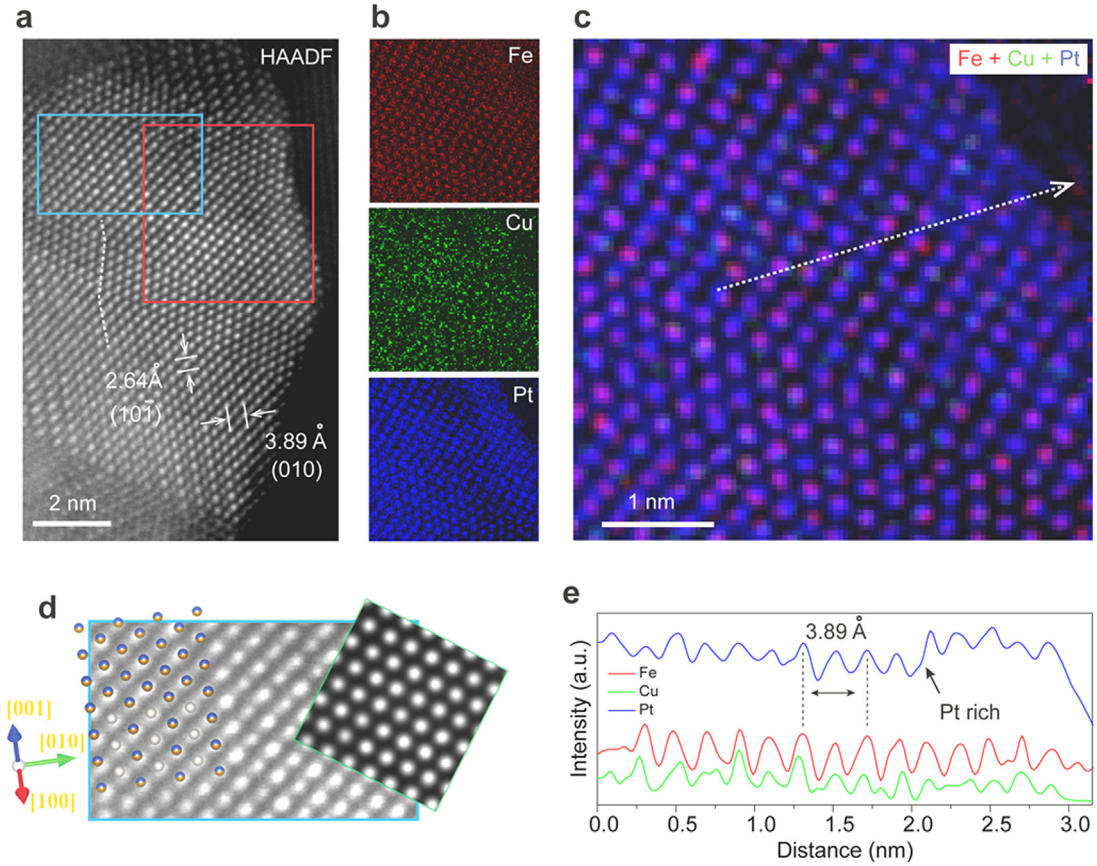

Fig. 5. Elemental distribution and surface analysis of $Fe_{45}Pt_{35}Cu_{20}$: a) Atomic resolution HAADF image of a surface region of the $Fe_{45}Pt_{35}Cu_{20}$ core–shell catalyst. b) Atomic resolution EELS mapping of red square region marked in Fig. 4a, and c) their overlaid image. d) An atomic model of $L1_0$–FePtCu and a simulated HAADF image of $L1_0$–FePtCu along [101] projection. (e) Atomically resolved elemental mapping images along [010] direction using EELS signal of Fe K (red), Cu K (green), Pt L (blue) edges, respectively. In this analyzed region, the surface termination is parallel to the (010) crystal plane of $L1_0$–FePtCu. At the particle surface, the Pt concentration increases indicating enrichment of Pt.

NPs, respectively, as shown in a high resolution image (Fig. S9 in Supporting information). These particles are ordered and with a well crystalline structure, which can be further confirmed by their FFT images. Thus, we may conclude that the better catalytic performance of $Fe_{45}Pt_{35}Cu_{20}$ is due to the composition optimization of a well–-crystallized core–shell structure with a Pt surface.

More interestingly, focusing on the shell of $Fe_{45}Pt_{35}Cu_{20}$ indicates an enrichment of platinum at its surface. Fig. 5a shows an atomic resolution image of a surface region of the $Fe_{45}Pt_{35}Cu_{20}$ core–shell catalyst. Fig. 5d is an enlarged image of the selected area marked by a blue rectangle. The STEM electron beam direction is parallel to the [101] crystal direction of $L1_0$–FePtCu. Along this crystal orientation, the Fe/Cu and Pt atoms are located in the same atomic column and in alternately distributed [101] direction. An atomic structure model of the tetragonal phase of FePtCu along the [101] projection and a simulated HAADF image were superimposed on the HAADF image. The surface termination of the particles is parallel to the (010) crystal plane of $L1_0$–FePtCu. Stacking faults can be observed as highlighted by the white dash lines in Fig. 5a. Fig. 5b and c shows the EELS elemental mapping of Fe, Cu and Pt and their overlay at atomic scale, in which the atom columns of each of the Fe and Pt elements are clearly resolved. Furthermore, comparing the intensity elemental mapping results reveals that there is a Pt enrichment layer (approximately 4–5 atomic layers) at the surface of core–shell structure, as can be seen from Fig. 5c. Fig. 5e shows the EELS line scan spectrum imaging of Fe K, Pt L, and Cu K of the arrow marked area in a region of Fig. 5c, which shows an obvious platinum enrichment at the surface with 5 atom layers. To carefully check these waves, we can see that the Fe, Cu, and Pt atoms are located in the same atom columns. This platinum enrichment finding is also confirmed by the EELS elemental mapping of other particles (Fig. S8 in Supporting information). Pt segregation at crystal surfaces have been reported previously for Pt-based alloys [40,58]. Preferential elemental segregation at the surface can result from differences in surface energy and/or atomic radius between the metal elements. An element with lower surface energy is more likely to segregate to the surface to minimize the overall Gibbs energy of a particle. Thus, larger Pt atoms (9.1 cm^3/mol) that diffuse to the outermost layer are energetically favored, thus releasing the elastic energy/strain in the antiparticles. The core–shell structure $Fe_{45}Pt_{35}Cu_{20}$ with 4–5 layers Pt surface not only exposes the stable $L1_0$–FePtCu shell with Pt enrichment surface to oxygen that is more robust than a Pt monolayer or alloy surfaces, but also offers desired core-shell interactions and alloy effects for optimal catalysis.

4. Conclusions

In conclusion, a facile polyol method was employed to prepare composition adjustable ordered $L1_0$–FePtCu NPs as active and stable ORR catalyst. The Cu alloying effect is the driving force of the $L1_0$–FePt ordering, which is effective up to a Cu content of 40%. Aberration-corrected STEM and X-ray diffraction provided insight into the composition effects on their ordering, core–shell/alloy structures, morphology and ORR performance. However, the particle size increases with the Fe or Cu ratio, and the particles are sintered for Fe (50%) and Cu (> 20%). The Fe and Cu content is critical to form a Cu/FePtCu core/shell structure, for Cu content with 20% ratio and Fe with more

than 40%. Optimized $Fe_{45}Pt_{35}Cu_{20}$ NPs with core–shell and a 4–5 atomic layer Pt-rich surface structure show better ORR catalysis performance than commercial Pt/C, or 4 times better mass activity and also good stability. The results demonstrate a facile new way to improve Pt catalysis for ORR and it will help to develop $L1_0$–FePt based core–-shell NPs for ORR for fuel cells and other electrochemical reactions. Our work provided a proof of a concept that high performance *fct*–FePt ORR catalyst are not only ordered, but also have a core–shell structure. Next steps to further enhance the catalysic performance may include using even smaller particle size and thinner shell thickness. Theoretical calculations could also be useful to elucidate the intrinsic relationship between the structure and the high electrocatalytic activities of Cu/FePtCu.

Acknowledgements

This work is supported by the National Natural Science Foundation of China (Grant No. 11574077). Xu Chen appreciates the China Scholarship Council's support (Grant No. 201708420175).

Appendix A. Supplementary material

Supplementary data associated with this article can be found in the online version at doi:10.1016/j.nanoen.2018.10.034.

References

[1] K.A. Kuttiyiel, Y. Choi, S.M. Hwang, G.G. Park, T.H. Yang, D. Su, K. Sasaki, P. Liu, R.R. Adzic, Nano Energy 13 (2015) 442–449.
[2] K.A. Kuttiyiel, Y. Choi, K. Sasaki, D. Su, S.M. Hwang, S.D. Yim, T.H. Yang, G.G. Park, R.R. Adzic, Nano Energy 29 (2016) 261–267.
[3] Y. Nie, L. Li, Z.D. Wei, Chem. Soc. Rev. 44 (2015) 2168–2201.
[4] Y.J. Wang, N.N. Zhao, B.Z. Fang, H. Li, X.T. Bi, H.J. Wang, Chem. Rev. 115 (2015) 3433–3467.
[5] L. Wu, A. Mendoza-Garcia, Q. Li, S.H. Sun, Chem. Rev. 116 (2016) 10473–10512.
[6] M.F. Li, Z.P. Zhao, T. Cheng, A. Fortunelli, C.Y. Chen, R. Yu, Q.H. Zhang, L. Gu, B.V. Merinov, Z.Y. Lin, E.B. Zhu, T. Yu, Q.Y. Jia, J.H. Guo, L. Zhang, W.A. Goddard, Y. Huang, X.F. Duan, Science 354 (2016) 1414–1419.
[7] D.H. Guo, R. Shibuya, C. Akiba, S. Saji, T. Kondo, J. Nakamura, Science 351 (2016) 361–365.
[8] X.Q. Huang, Z.P. Zhao, L. Cao, Y. Chen, E.B. Zhu, Z.Y. Lin, M.F. Li, A.M. Yan, A. Zettl, Y.M. Wang, X.F. Duan, T. Mueller, Y. Huang, Science 348 (2015) 1230–1234.
[9] Q.H. Li, W.X. Chen, H. Xiao, Y. Gong, Z. Li, L.R. Zheng, X.S. Zheng, W.S. Yan, W.C. Cheong, R.A. Shen, N.H. Fu, L. Gu, Z.B. Zhuang, C. Chen, D.S. Wang, Q. Peng, J. Li, Y.D. Li, Adv. Mater. 30 (2018) 1800588.
[10] H.T. Chung, D.A. Cullen, D. Higgins, B.T. Sneed, E.F. Holby, K.L. More, P. Zelenay, Science 357 (2017) 479–484.
[11] X. Yang, L.T. Roling, M. Vara, A.O. Elnabawy, M. Zhao, Z.D. Hood, S.X. Bao, M. Mavrikakis, Y.A. Xia, Nano Lett. 16 (2016) 6644–6649.
[12] Z.Q. Niu, N. Becknell, Y. Yu, D. Kim, C. Chen, N. Kornienko, G.A. Somorjai, P.D. Yang, Nat. Mater. 15 (2016) 1188–1195.
[13] L. Gan, C. Cui, M. Heggen, F. Dionigi, S. Rudi, P. Strasser, Science 346 (2014) 1502–1506.
[14] A.M. Gomez-Marin, J.M. Feliu, Catal. Today 244 (2015) 172–176.
[15] Y.H. Han, Y.G. Wang, W.X. Chen, R.R. Xu, L.R. Zheng, J. Zhang, J. Luo, R.A. Shen, Y.Q. Zhu, W.C. Cheong, C. Chen, Q. Peng, D.S. Wang, Y.D. Li, J. Am. Chem. Soc. 139 (2017) 17269–17272.
[16] Y.J. Chen, S.F. Ji, C. Chen, Q. Peng, D.S. Wang, Y.D. Li, Joule 2 (2018) 1242–1264.
[17] A.J. Han, W.X. Chen, S.L. Zhang, M.L. Zhang, Y.H. Han, J. Zhang, S.F. Ji, L.R. Zheng, Y. Wang, L. Gu, C. Chen, Q. Peng, D.S. Wang, Y.D. Li, Adv. Mater. 30 (2018) 1706508.
[18] Y.H. Han, Y.G. Wang, R.R. Xu, W.X. Chen, L.R. Zheng, A.J. Han, Y.Q. Zhu, J. Zhang, H.B. Zhang, J. Luo, C. Chen, Q. Peng, D.S. Wang, Y.D. Li, Energy Environ. Sci. 11 (2018) 2348–2352.
[19] R. Lin, X. Cai, H. Zeng, Z.P. Yu, Adv. Mater. 30 (2018) 1705332.
[20] S. Sui, X.Y. Wang, X.T. Zhou, Y.H. Su, S. Riffatc, C.J. Liu, J. Mater. Chem. A 5 (2017) 1808–1825.
[21] H.F. Lv, D.G. Li, D. Strmcnik, A.P. Paulikas, N.M. Markovic, V.R. Stamenkovic, Nano Energy 29 (2016) 149–165.
[22] Y.C. Zeng, Z.G. Shao, H.J. Zhang, Z.Q. Wang, S.J. Hong, H.M. Yu, B.L. Yi, Nano Energy 34 (2017) 344–355.
[23] W. Ye, S.M. Chen, M.S. Ye, C.H. Ren, J. Ma, R. Long, C.M. Wang, J. Yang, L. Song, Y.J. Xiong, Nano Energy 39 (2017) 532–538.
[24] Q.L. Chen, Z.M. Cao, G.F. Du, Q. Kuang, J. Huang, Z.X. Xie, L.S. Zheng, Nano Energy 39 (2017) 582–589.
[25] J. Li, H.M. Yin, X.B. Li, E. Okunishi, Y.L. Shen, J. He, Z.K. Tang, W.X. Wang, E. Yücelen, C. Li, Y. Gong, L. Gu, S. Miao, L.M. Liu, J. Luo, Y. Ding, Nat. Energy 2 (2017) 17111.
[26] Y. Xiong, L. Xiao, Y. Yang, F.J. DiSalvo, H.D. Abruna, Chem. Mater. 30 (2018) 1532–1539.
[27] X.L. Tian, J.M. Luo, H.X. Nan, H.B. Zou, R. Chen, T. Shu, X.H. Li, Y.W. Li, H.Y. Song, S.J. Liao, R.R. Adzic, J. Am. Chem. Soc. 138 (2016) 1575–1583.
[28] P. Strasser, M. Gliech, S. Kuehl, T. Moeller, Chem. Soc. Rev. 47 (2018) 715–735.
[29] D.S. Choi, A.W. Robertson, J.H. Warner, S.O. Kim, H. Kim, Adv. Mater. 28 (2016) 7115–7122.
[30] D.L. Wang, H.L. Xin, R. Hovden, H.S. Wang, Y.C. Yu, D.A. Muller, F.J. DiSalvo, H.D. Abruna, Nat. Mater. 12 (2013) 81–87.
[31] B.W. Zhang, Z.C. Zhang, H.G. Liao, Y. Gong, L. Gu, X.M. Qu, L.X. You, S. Liu, L. Huang, X.C. Tian, R. Huang, F.C. Zhu, T. Liu, Y.X. Jiang, Z.Y. Zhou, S.G. Sun, Nano Energy 19 (2016) 198–209.
[32] S.F. Liu, W.P. Xiao, J. Wang, J. Zhu, Z.X. Wu, H.L. Xin, D.L. Wang, Nano Energy 27 (2016) 475–481.
[33] J. Kim, Y. Lee, S.H. Sun, J. Am. Chem. Soc. 132 (2010) 4996–4997.
[34] V.R. Stamenkovic, B. Fowler, B.S. Mun, G.F. Wang, P.N. Ross, C.A. Lucas, N.M. Markovic, Science 315 (2007) 493–497.
[35] K.D. Gilroy, X. Yang, S.F. Xie, M. Zhao, D. Qin, Y.N. Xia, Adv. Mater. 30 (2018) 1706312.
[36] M. Gocyla, S. Kuehl, M. Shviro, H. Heyen, S. Selve, R.E. Dunin-Borkowski, M. Heggen, P. Strasser, ACS Nano 12 (2018) 5306–5311.
[37] V. Beermann, M. Gocyla, S. Kuhl, E. Padgett, H. Schmies, M. Goerlin, N. Erini, M. Shviro, M. Heggen, R.E. Dunin-Borkowski, D.A. Muller, P. Strasser, J. Am. Chem. Soc. 139 (2017) 16536–16547.
[38] G.M. Jiang, H.Y. Zhu, X. Zhang, B. Shen, L.H. Wu, S. Zhang, G. Lu, Z.B. Wu, S.H. Sun, ACS Nano 9 (2015) 11014–11022.
[39] X.L. Sun, D.G. Li, Y. Ding, W.L. Zhu, S.J. Guo, Z.L. Wang, S.H. Sun, J. Am. Chem. Soc. 136 (2014) 5745–5749.
[40] C. Chen, Y.J. Kang, Z.Y. Huo, Z.W. Zhu, W.Y. Huang, H.L. Xin, J.D. Snyder, D.G. Li, J.A. Herron, M. Mavrikakis, M.F. Chi, K.L. More, Y.D. Li, N.M. Markovic, G.A. Somorjai, P.D. Yang, V.R. Stamenkovic, Science 343 (2014) 1339–1343.
[41] J. Zhang, K. Sasaki, E. Sutter, R.R. Adzic, Science 315 (2007) 220–222.
[42] S.J. Guo, S. Zhang, S.H. Sun, Angew. Chem. Int. Ed. 52 (2013) 8526–8544.
[43] Q. Li, L.H. Wu, G. Wu, D. Su, H.F. Lv, S. Zhang, W.L. Zhu, A. Casimir, H.Y. Zhu, A. Mendoza-Garcia, S.H. Sun, Nano Lett. 15 (2015) 2468–2473.
[44] W.P. Xiao, M.A.L. Cordeiro, G.Y. Gao, A.M. Zheng, J. Wang, W. Lei, M.X. Gong, R.Q. Lin, E. Stavitski, H.L. Xin, D.L. Wang, Nano Energy 50 (2018) 70–78.
[45] S. Zhang, X. Zhang, G.M. Jiang, H.Y. Zhu, S.J. Guo, D. Su, G. Lu, S.H. Sun, J. Am. Chem. Soc. 136 (2014) 7734–7739.
[46] X. Chen, Y. Wang, H.B. Wang, D. Shu, J. Zhang, P. Ruterana, H. Wang, J. Mater. Chem. C. 5 (2017) 5316–5322.
[47] H.B. Wang, P.J. Shang, J. Zhang, M.W. Guo, Y.P. Mu, Q. Li, H. Wang, Chem. Mater. 25 (2013) 2450–2454.
[48] Y. Yu, P. Mukherjee, Y. Tian, X.Z. Li, J.E. Shield, D.J. Sellmyer, Nanoscale 6 (2014) 12050–12055.
[49] W. Yang, W. Lei, Y. Yu, W. Zhu, T.A. George, X.Z. Li, D.J. Sellmyer, S.H. Sun, J. Mater. Chem. C 3 (2015) 7075–7080.
[50] W. Yang, Y. Yu, L. Wang, C. Yang, H. Li, Nanoscale 7 (2015) 2877–2882.
[51] W. Lei, Y. Yu, W. Yang, M. Feng, H. Li, Nanoscale 9 (2017) 12855–12961.
[52] W. Wang, Z.Y. Wang, M.M. Yang, C.J. Zhong, C.J. Liu, Nano Energy 25 (2016) 26–33.
[53] C. Wang, H. Daimon, T. Onodera, T. Koda, S.H. Sun, Angew. Chem. 120 (2008) 3644–3647.
[54] A.S. Arico, S. Srinivasan, V. Antonucci, Fuel Cells 1 (2001) 133–161.
[55] W. Chen, J.M. Kim, S.H. Sun, S.W. Chen, Langmuir 23 (2007) 11303–11310.
[56] S. Kukunuri, K. Naik, S. Sampath, J. Mater. Chem. A 5 (2017) 4660–4670.
[57] D.A. Gilbert, L.W. Wang, T.J. Klemmer, J.U. Thiele, C.H. Lai, K. Liu, Appl. Phys. Lett. 102 (2013) 132406.
[58] R.M. Wang, O. Dmitrieva, M. Farle, G. Dumpich, H.Q. Ye, H. Poppa, R. Kilaas, C. Kisielowski, Phys. Rev. Lett. 100 (2008) 017205.